Resonant tunneling in graphene pseudomagnetic quantum dots

— Supporting information —

Zenan Qi,[1] D. A. Bahamon,[2] Vitor M. Pereira,[2,*] Harold S. Park,[1] D. K. Campbell,[3] and A. H. Castro Neto[2,3]

[1]*Department of Mechanical Engineering, Boston University, Boston, MA 02215*

[2]*Graphene Research Centre & Department of Physics, National University of Singapore, 2 Science Drive 3, Singapore 117542*

[3]*Department of Physics, Boston University, Boston, MA 02215, USA*

(Dated: May 8, 2013)

*Corresponding author: vpereira@nus.edu.sg

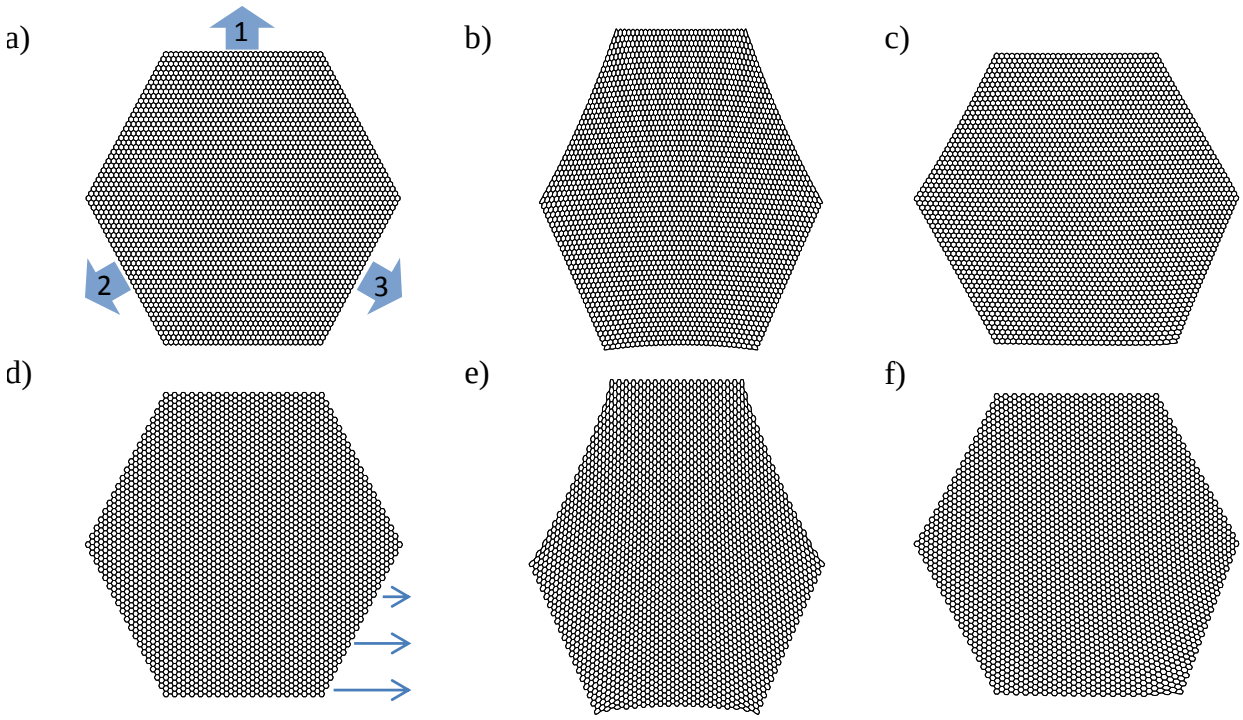

FIG. 1: (a) Hexagon (0% strain) with ZZ edges. The arrows are a schematic representation of the symmetrically applied tri-axial strain. In the transport calculations the contacts are attached to the edges under traction as well because the edge atoms are held fixed along the direction transverse to the tension, which allows us to keep the metallic contacts undeformed. (b) Deformed hexagon with ZZ edges after 10% of symmetric strain. (c) Deformed hexagon with ZZ edges after 15% of asymmetric (ramp) strain. (d) Hexagon (0% strain) with AC edges. The arrows are a schematic representation of the asymmetrical (ramp) strain setup. (e) Deformed hexagon with AC edges under 15% of symmetric strain. (f) Deformed hexagon with AC edges under 15% of asymmetric (ramp) strain.

I. DEFORMED HEXAGONS UNDER STRAIN

The graphene hexagon was deformed via molecular mechanics using the open-source atomistic simulation package LAMMPS [1], where molecular mechanics implies deformation at 0K. The C-C interactions were modeled using the Adaptive Intermolecular Reactive Empirical Bond Order (AIREBO) potential [2]

$$E = \frac{1}{2}\sum_{i}\sum_{j\neq i}\left[E_{ij}^{REBO} + E_{ij}^{LJ} + \sum_{k\neq i,j}\sum_{l\neq i,j,k} E_{kijl}^{TORSION}\right], \tag{1}$$

which consists of three parts: the 2nd generation REBO potential (E_{ij}^{REBO}) [3], a standard Lennard Jones potential (E_{ij}^{LJ}), and a many body torsion term ($E_{kijl}^{TORSION}$). As shown in Eq. (1), E^{REBO} is the 2nd generation Brenner potential which dominates the short-range

interactions. The Lennard-Jones E^{LJ} term is only switched on for long-range interactions between 0.2 nm to the cut-off radius of the interatomic potential (0.68 nm), and is switched off for distances shorter than 0.2 nm to avoid its steep ($1/r_{ij}^{12}$) repulsive wall. Finally, the $E^{TORSION}$ term depends on dihedral angles which have little effect in this work due to the 2D nature of graphene. No periodic boundary conditions were used in this work, and the total numbers of atoms used in the zigzag and armchair sheets are 6144 and 6162, respectively. We define three edge groups (32 atoms in each group for zigzag, 38 atoms in each group for armchair) and applied displacement loading to the three edges as shown in Fig. 1(a). For asymmetric loading cases, one edge was stretched while the other two were fixed, as illustrated in Fig. 1(d).

Since molecular mechanics simulations are performed at 0K, there is no need for thermostats to control the temperature of the system, and the equilibrium (minimum energy) positions of the atoms are obtained using the conjugate gradient method with a relative energy tolerance of 10^{-7} eV between successive displacement increments. Specifically, the graphene hexagon is stretched by applying displacement increments of 0.01 Å perpendicular to the corresponding edges, as illustrated in Fig. 1(a). After the displacement increment is applied to the three edges, the three edges are held fixed, at which point the unconstrained atoms in the hexagon are allowed to relax to their corresponding equilibrium positions using the conjugate gradient algorithm. This stretching and relaxation loop is repeated until the desired nominal strain (ϵ_{eff}) is reached. Fracture of the hexagonal sheet is observed when ϵ_{eff} goes up to $\sim$19% for the symmetric loading depicted in Fig. 1(a). Fig. 1 shows the hexagonal quantum dots considered in this study under different loading conditions and for different lattice orientations with respect to the applied strain. The strategy used to explore deviations from the symmetric loading is shown schematically in Fig. 1(d). In this case the traction is applied only to edge 3, and in such a way that the displacement follows a ramp pattern, being maximal at one end of the edge and linearly decreasing to zero towards the opposite end. Edges 1 and 2 are held fixed Figs 1c and 1f show the actual relaxed structures after the molecular mechanics simulation under this ramp traction profile, and for 15% of nominal strain applied to the lower atoms.

II. ARMCHAIR Y-JUNCTION

The electronic spectrum and transport characteristics of graphene nanostructures is strongly influenced by the nature of the edges. Strain-induced PMFs also depend on the relative orientation of the strain with respect to the underlying crystal directions of the graphene lattice. Here we consider a quantum dot with the same geometry and the same approximate dimensions as the one discussed in the main text, but for which the graphene lattice has been rotated so that the edges are now of the armchair (AC) type. This corresponds to a rotation of the original lattice by $\pi/2$, or any other equivalent angle.

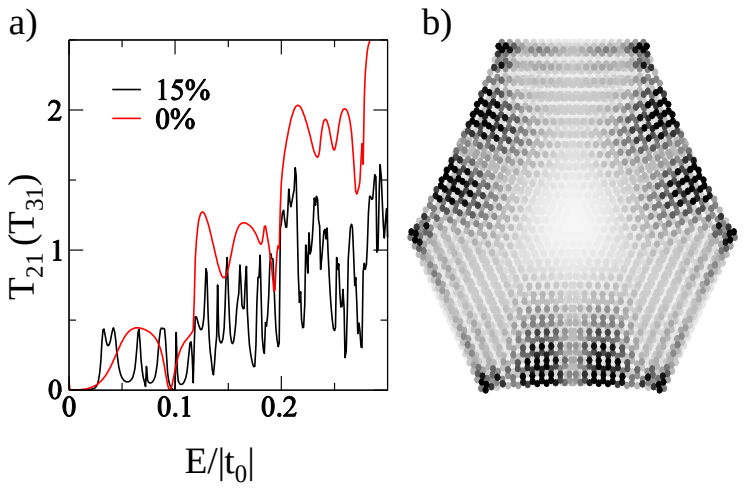

FIG. 2: (Color online) (a) Transmission coefficient $T_{21}(T_{31})$ *vs* Fermi Energy for a symmetrically strained AC Y-junction. (b) LDOS mapping at $E = 0.043t_0$ for the 15% symmetrically strained AC Y-junction.

The calculation of the transmission is done now by attaching three unstrained semi-infinite zig-zag (ZZ) graphene nanoribbons, which act as ideal contacts. As in the main text, the contacts are connected to the sides of the hexagon where the load is applied, creating an AC Y-junction. In Fig. 2(a) we can see the transmission coefficient for 0% strain (red). As discussed in the main text for the ZZ case, the onset of transmission in the unstrained structure is characterized by a very broad hump, that is associated with the fundamental mode of the cavity. The different nature of the AC edges manifests itself by the wider and deeper resonances and anti-resonances that develop as the energy increases, in comparison with the transmission fingerprint of the unstrained ZZ junction discussed in the main text. When strain is applied up to the nominal value of 10% the transmission coefficient mostly resembles the unstrained case, and the case of $\epsilon_{\text{eff}} = 15\%$, represented by the black curve in Fig. 2(a) is still qualitatively similar to the unstrained situation. More specifically, despite the additional structure, there are no isolated resonant peaks in contrast to the case of the ZZ junction, and transmission is never zero after the initial onset at around $E \simeq 0.02$. In clear contrast with the case analyzed in the main text, the transmission signature of this junction is not compatible with the presence of a significant pseudomagnetic field within the central region of the hexagon. Direct inspection of the real-space LDOS distribution at the transmission peaks confirms this. Fig. 2(b) represents a density plot of the LDOS for the transmission peak at $E = 0.043t_0$, revealing a LDOS distribution qualitatively similar to any resonance in the unstrained structure.

The inference that there is no significant homogeneous magnetic field within the junction from the transport fingerprint alone is compatible with the expectation for the pseudomagnetic field distribution anticipated in this case. Despite the generic relevance of the edge

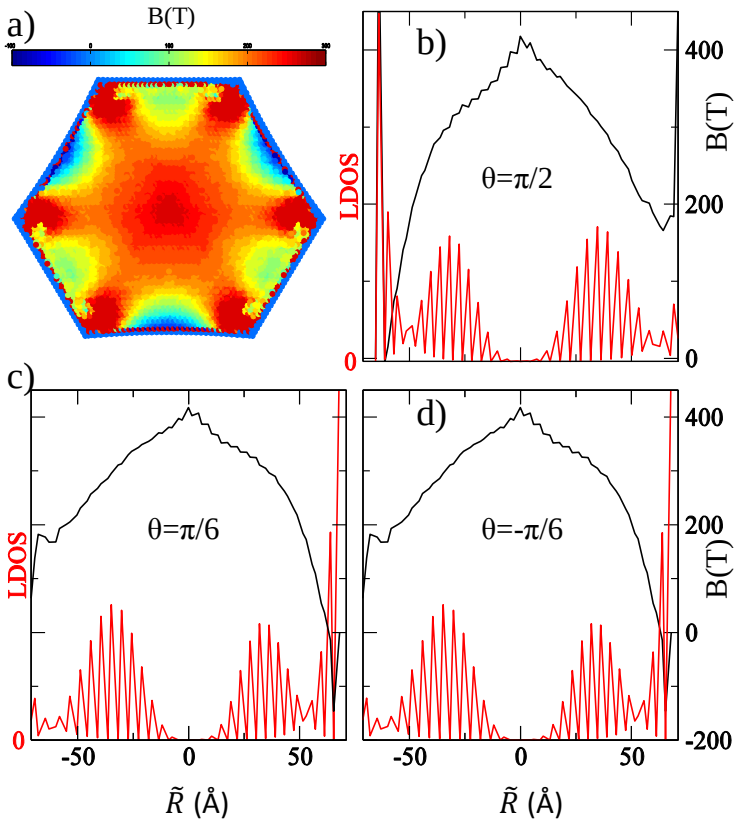

FIG. 3: (Color online) Sections of B_s and LDOS for a strained ZZ Y-junction with $\epsilon_{\text{eff}} = 10\%$. Panel (a) shows a density plot of B_s in the entire system obtained with the "displacement approach". In panels (b)-(d) we plot the profile of B_s (black) and LDOS (red) at $E = 0.018t_0$ along the directions defined in the text: $\theta = \pi/2$, $\theta = \pi/6$, and $\theta = -\pi/6$, respectively.

chirality in small graphene structures, the crucial detail in the context of generating suitable PMF distributions is the orientation of the lattice with respect to the strain directions. On the basis of the results derived in reference 4 we can expect the magnitude of the PMF near the center of the hexagon to vary with the lattice orientation as $\propto \cos(3\varphi)$, where $\varphi = 0$ corresponds to a lattice with a ZZ direction along the horizontal axis. Since the AC case studied in Fig. 2 corresponds to $\varphi = \pi/6, \pi/2$, etc. we expect the magnitude of the pseudomagnetic field to be mostly suppressed in the central region.

III. PROFILE OF B_s AND LDOS (ZZ JUNCTION)

In the main text we studied in detail the case of a ZZ junction under $\epsilon_{\text{eff}} = 10\,\%$. From the nature of the resonant transmission at low energies, and from the equidistant spacing between resonances, we extracted an average pseudomagnetic field B_s^{av} determining the behavior of transmission. Moreover, we stated that the resonant transmission occurs only through the assistance of those edge states whose radius is such that they effectively couple

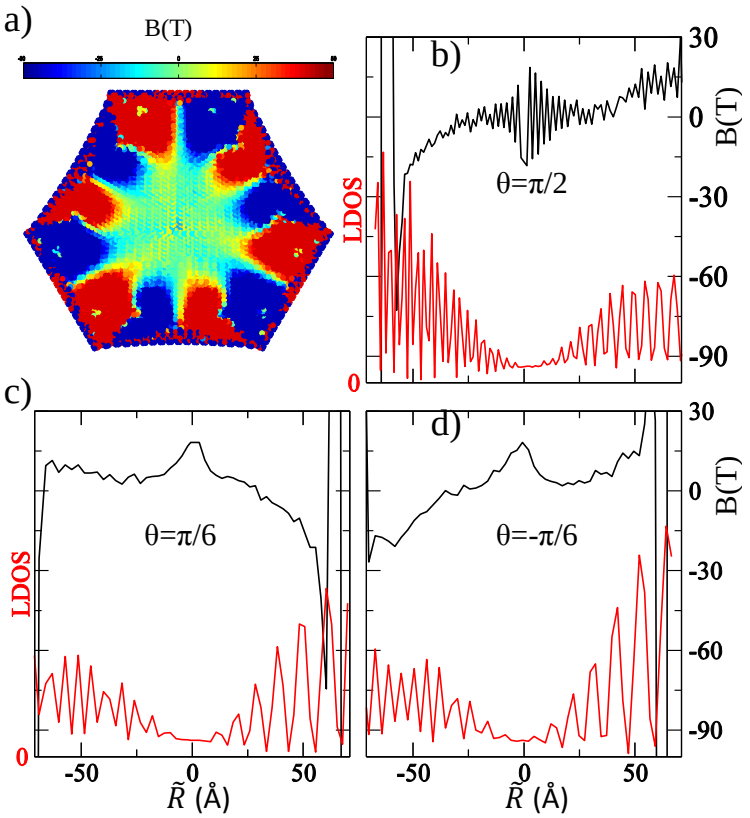

FIG. 4: Sections of B_s and LDOS for a strained AC Y-junction with $\epsilon_{\text{eff}} = 15\%$. Panel (a) shows a density plot of B_s in the entire system obtained with the "displacement approach". In panels (b)-(d) we plot the profile of B_s (black) and LDOS (red) at $E = 0.043t_0$ along the directions defined in the text: $\theta = \pi/2$, $\theta = \pi/6$, and $\theta = -\pi/6$, respectively.

to the contacts at the border.

To clarify these points, the values of B_s and LDOS at $E_1 = 0.018t_0$ in the ZZ junction with $\epsilon_{\text{eff}} = 10\%$, are extracted along transverse sections equivalent by symmetry. The origin of coordinates is set at the center of the strained hexagon, with the x and y axes along the conventional horizontal and vertical directions. The direction of the transverse section with respect to the horizontal axis is defined by the angle θ, and the position of a point in the lattice along this section is identified by $\tilde{R} = \text{sign}(y)\sqrt{x^2 + y^2}$. We shall consider the three equivalent transverse sections along $\theta = \pi/2$ and $\pm\pi/6$. For example, contact 1 appears at $\tilde{R} \approx 74\,\text{Å}$ in a section taken along $\theta = \pi/2$. These three sections are chosen to confirm and highlight the isotropy of both B_s and the LDOS in the interior of the structure.

The overall distribution of B_s within the hexagon is shown in Fig. 3(a). The value of B_s shown here is extracted using the "displacement" approach discussed in the main text. It consists in using the coordinates of the relaxed atoms directly to interpolate the strain tensor, after which the vector potential $\boldsymbol{A}_s$ is extracted. This method has the potential disadvantage of requiring a sequence of three numerical derivatives to obtain the value of

B_s at a given lattice point, given the relaxed atomic coordinates, and also overestimates B_s at large deformations, as shown in Fig. 3 of the main text. However it is much more expedite than the mapping of the LDOS, and extraction of the local LL spectrum from the tight-binding calculation, which was the method used to plot B_s in Fig. 1 of the main text. Correcting for the overestimate in magnitude discussed and shown in Fig. 3 of the main text, the distribution of B_s obtained with either method in the interior of the structure is equivalent.

The values of B_s and LDOS along the three sections mentioned above are plotted in Figs. 3(b)-(d), represented by the black traces. The LDOS is plotted together with the pseudomagnetic field along the three sections, represented by the red traces. First, we notice that the large peaks located at boundary $\tilde{R} = -65\,\text{Å}$ ($\theta = \pi/2$), $\tilde{R} = 68\,\text{Å}$ ($\theta = \pi/6$), and $\tilde{R} = 68\,\text{Å}$ ($\theta = -\pi/6$) are due to ZZ edge states. At the opposite boundary (where the contacts are attached) the LDOS is small, signaling that this state is well confined within the interior of the structure, and that the probability of transmission through it is small. The most interesting detail of the LDOS distribution, however, is its distribution in the interior of the structure. It is clear that the wave function does not follow local features in B_s, such as changes of strength or sign of B_s [5]. In contrast, the LDOS intensity is almost completely confined to an annular region inside the junction, fully resembling the LDOS of an edge state in a magnetic quantum dot, as described by Lent [6]. From the LDOS profile we obtain $\ell_{B_s} \approx 2\,\text{nm}$, which corresponds to the average field $B_s^{\text{av}} = \hbar/el_{B_s}^2 \simeq 164\,\text{T}$ extracted in the main text.

IV. PROFILE OF B_s AND LDOS (AC JUNCTION)

The procedure described in the previous section is applied to the analysis of the AC junction with $\epsilon_{\text{eff}} = 15\%$. As expected, the magnitude of B_s is roughly zero in the interior region of the junction. Sharp features appear only around small regions near the corners and edges, where the field is strong and alternates in sign. Figs. 4(b)-(d) show the profile of B_s together with the LDOS at $E = 0.043t_0$, the same energy used in Fig. 2 above.

V. EDGE ROUGHNESS AND ASYMMETRIC STRAIN

In order to simulate the effect of edge roughness, vacancies were added with a probability of 0.4 to the edges of the two types of Y-junction. These vacancies were added in the strained electronic Hamiltonian neglecting the relaxation of local strain in the vicinity of the vacancy. This simplification should not modify our results since the main ingredient is that edge roughness reduces the transmission through pseudo-magnetic edge states (standing waves in the strain barrier) for ZZ edged Y-junctions, as can be seen in Fig. 5(a). In these structures the B_s in the interior of the junction behaves like a barrier, pushing the current towards the

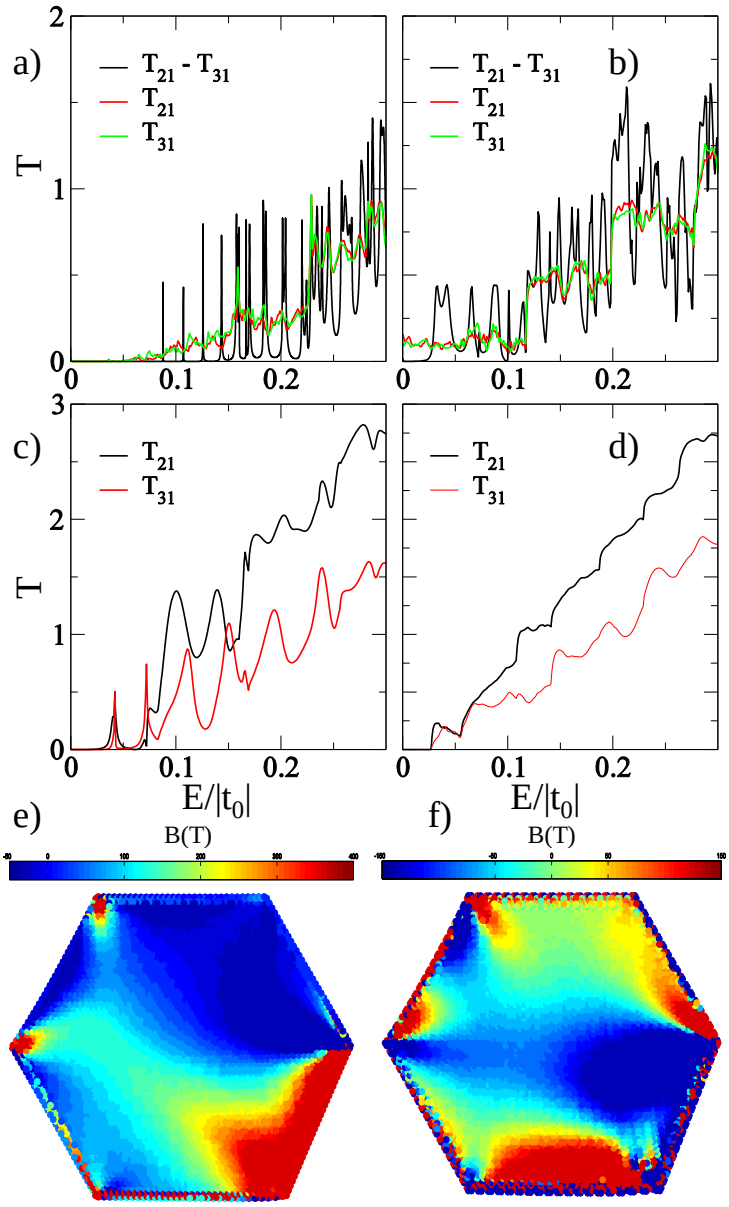

FIG. 5: Transmission coefficient for: (a) 10% strained ZZ Y-junction with and without edge disorder; (b) 15% strained AC Y-junction with and without edge disorder; (c) 15% asymmetrically strained ZZ Y-junction; (d) 15% asymmetrically strained ZZ Y-junction with edge disorder. In panels (e) and (f) we display the distribution of B_s generated by the asymmetric traction illustrated in Fig. 1(d) for the case of, respectively, the ZZ and AC edged hexagon nanostructures considered in this work.

edges. This current is effectively suppressed at low energies by the strong backscattering induced by the vacancies. This creates the gap in transmission at low energies that can be seen in Fig. 5(a). In the AC-edged hexagonal dot, since the average $B_s \approx 0$ in the center of the Y-junction, current flows easily through the central region, and there is no transmission

gap.

To address the problem of asymmetry in the traction (and consequently in the overall strain distribution), we consider the extremely asymmetric situations illustrated in Figs. 1(c) and (f). The transmission data is shown in Fig. 5(c), for a structure where a ramp displacement is applied only to the hexagon side where the third contact is attached. An asymmetric strain pattern ensures that $T_{21} \neq T_{31}$, and can potentially be explored to channel the current between specific pairs of contacts by suitable asymmetric traction conditions. The ramp strain considered here creates a B_s that is not uniform in the center of the hexagon, but has a strong maximum in the vicinity of the third contact. Although the values of B_s in that region are large ($\ell_{B_s} < L_0$), and of the same order of magnitude as the ones found in the symmetric junction, the transmission and LDOS signatures are rather different from the signatures of a symmetrically strained hexagon. In particular the resonant peaks in T_{31} at $E = 0.042t_0$ and $E = 0.072t_0$ are due to states having a LDOS distribution of two distorted standing waves, rather than the magnetic edge state profiles seen in the symmetric case in Fig. 3. The reason for the different behavior is mostly due to the non-uniform nature of B_s in the interior of the system, in comparison with the symmetrically strained situation. This means that the electrons don't feel a quantum dot with a nearly constant magnetic field everywhere in this case, but instead are scattered from the regions of higher field.

In essence, this extreme asymmetric case results in a distribution of B_s that acts as a barrier for current flow only in certain regions inside the Y-junction. Since that barrier is higher in the region of contact 3 the current is scattered to contact 2 and, consequently, $T_{31} < T_{21}$. This imbalance in T_{31} vs T_{21} becomes even more evident at higher energies. Inside the ZZ Y-junction, for low energies, the current flows through the regions of low B_s, as shown in more detail the next section of this supporting information.

The effect of edge disorder in the asymmetric ZZ junction is presented in Fig. 5(d), where we see that the effect is not as marked as in the symmetric case shown in Fig. 5(a). This is consistent with the above description of the transmission process in this case, whereby electronic current flows through the large portions of the hexagon that are not under a significant B_s.

VI. B_s AS A BARRIER

The current between neighboring sites m and n can be expressed as [7, 8]

$$I_{mn} = \frac{2e}{h} \int_{-\infty}^{+\infty} dE[t_{nm}G^{<}_{mn} - t_{mn}G^{<}_{nm}], \tag{2}$$

where the lesser Green's function in the absence of interactions can be written as $G^{<}(E) = G^{r}(E)[\Gamma_1 f_1 + \Gamma_2 f_2 + \Gamma_3 f_3]G^{a}(E)$. $f_{1(2)(3)}$ is the Fermi distribution in the respective electrodes. We mapped the current density for different energies for the ZZ and AC Y-junction with symmetric and asymmetric strain. For reference, we shown in Fig. 6 the current maps for

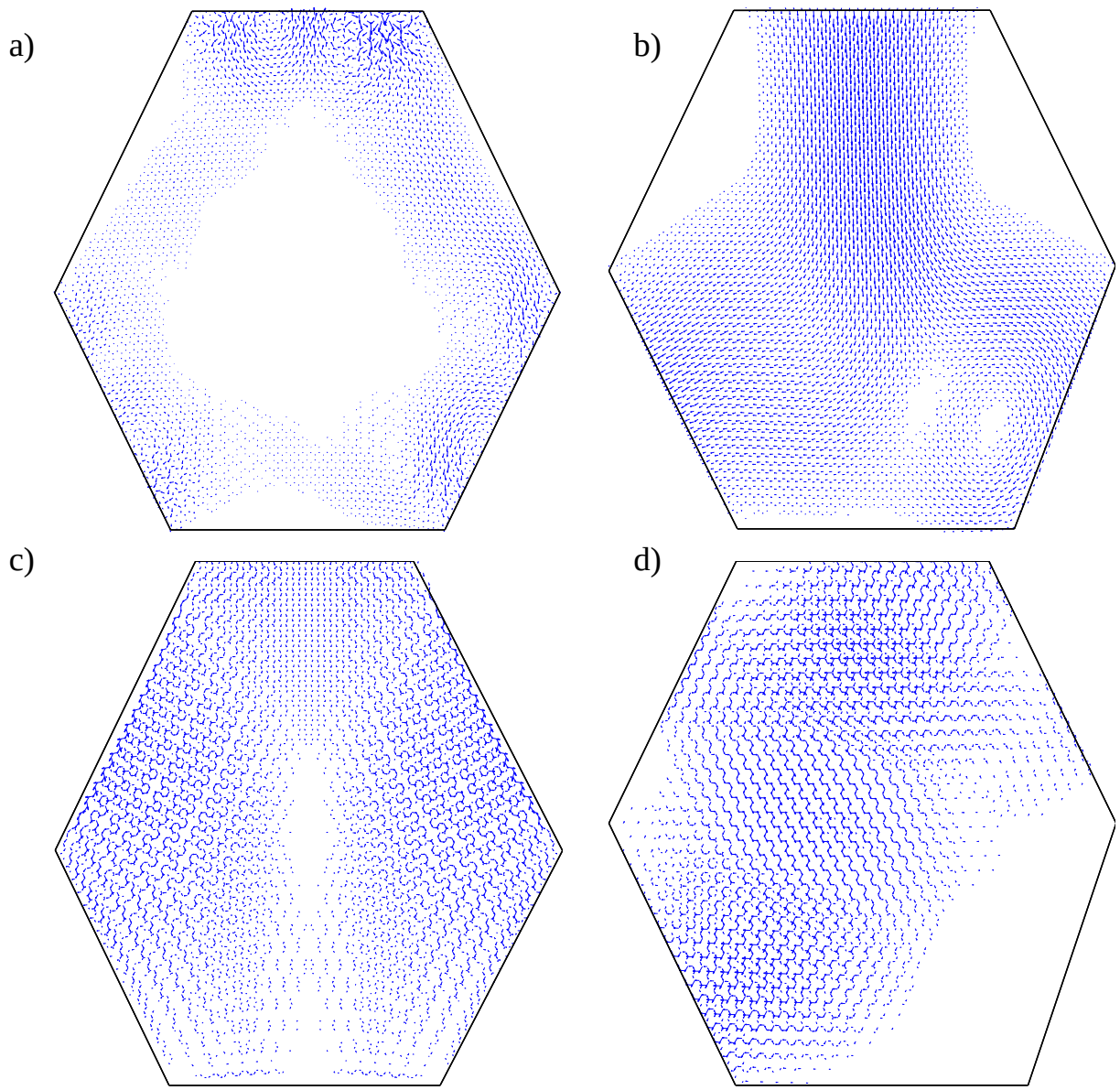

FIG. 6: Current density mapping in real space for selected transmission features discussed in the main text and above: (a) $E = 0.126t_0$ for the symmetric ZZ Y-junction with $\epsilon_{\text{eff}} = 10\%$; (b) for the asymmetrically strained ZZ Y-junction with $\epsilon_{\text{eff}} = 15\%$ at $E = 0.1t_0$; (c) at $E = 0.033t_0$ for the symmetric AC Y-junction with $\epsilon_{\text{eff}} = 15\%$; (d) for the asymmetrically strained AC Y-junction at $E = 0.095t_0$. In all plots, the length of the arrow is proportional to the value of the density current in that point.

some of the cases discussed in the main text, as well as in the previous sections of this supporting information.

The case plotted in Fig. 6(a) pertains to a symmetrically strained ZZ Y-junction, at the energy $E = 0.126t_0$ that corresponds to one of the isolated transmission resonances. Since

B_s is strong in most of the interior region the current path exhibits the intuitively expected behavior by flowing through the regions of smallest field towards the edges. Due to the microscopic details of B_s the current density distribution is not perfectly symmetric between contacts 1–2 and contacts 1–3. A higher density of current flows between 1–3, and part of it is scattered from contact 3 to contact 2 ensuring final transmissions of $T_{21}(0.126t_0) = 0.31 \approx T_{31}(0.126t_0) = 0.32$.

For the asymmetrically strained ZZ Y-junction in Fig. 6(b) the bulk of the current flows directly through the center of the junction, exiting predominantly via contact 2. Most of the current near contact 3 is scattered towards 2, since in the asymmetric ZZ case the magnetic barrier induced by B_s is displaced to the vicinity of 3. This explains the quantitative imbalance in the respective transmissions: $T_{21}(0.1t_0) = 1.37 > T_{31}(0.1t_0) = 0.47$ [cfr. Fig. 5(c). The qualitative picture is similar for the AC Y-junction asymmetrically strained by 15% in Fig. 6(d). The main point is that under asymmetric traction conditions the distribution of B_s is no longer nearly homogeneous in the central region, and a strong maximum appears towards one of the pulling arms. This restricts the magnetic barrier to a particular portion of the system, but does not lead to the Landau level assisted tunneling resonances seen in the symmetric ZZ case, and discussed in the main text. The asymmetric cases can be understood intuitively by considering the regions of strong B_s as barriers that divert the electronic current, and lead to an asymmetry in the conductance measured between contacts 1–2 and 1–3.

For completeness in Fig. 6(c) we show the current density in a 15% symmetrically strained AC Y-junction, extracted at a maximum in the transmission at $E = 0.033t_0$.

---

[1] Lammps, http://lammps.sandia.gov (2012).

[2] S. J. Stuart, A. B. Tutein, and J. A. Harrison, J. Chem. Phys. **112**, 6472 (2000).

[3] D. W. Brenner, O. A. Shenderova, J. A. Harrison, S. J. Stuart, B. Ni, and S. B. Sinnott, Journal of Physics: Condensed Matter **14**, 783 (2002).

[4] F. Guinea, M. I. Katsnelson, and A. K. Geim, Nat Phys **6**, 30 (2010).

[5] M. R. Masir, P. Vasilopoulos, and F. M. Peeters, Journal of Physics: Condensed Matter **23**, 315301 (2011).

[6] C. S. Lent, Phys. Rev. B **43**, 4179 (1991).

[7] S. Datta, *Electronic Transport in Mesoscopic Systems* (Cambridge University Press., 1995).

[8] D. A. Bahamon, A. L. C. Pereira, and P. A. Schulz, Phys. Rev. B **83**, 155436 (2011).